



Cite this: DOI: 10.1039/d1tc06171b

Light-modulated liquid crystal elastomer actuator with multimodal shape morphing and multifunction†

Tonghui Zhao,^{a,b,c} Yanlin Zhang,^{b,c} Yangyang Fan,^{b,c} Jiao Wang,^{a,b,c} Hanqing Jiang^{b,c} and Jiu-an Lv ^{b,c*}

Stimulus-responsive materials provide an attractive platform to design and build distinguished soft robots that can dynamically change their shapes to adapt for a variety of functions. However, in most cases, soft robots mainly rely on delicately and laboriously tailoring material composition and molecular orientations to achieve desirable shape morphing. Moreover, the integration of multimodal shape morphing into a single robot, control of the evolution between different morphing modes, complex locomotion, and facile fabrication represent major challenges in this area. Here, we show a facile strategy to photomanipulate shape morphing of a soft millirobot made of an NIR-active liquid crystal elastomer by programming the direction and magnitude of strain gradient in the LCE by using the spatial and localized features of light stimuli. This photomanipulation strategy not only enables the millirobot to generate a wide range of morphing modes, but also allows local and reversible evolution between different morphing modes in a single soft robot. With these phototunable morphing capabilities, the millirobot is able to exert multimodal locomotive behaviors, including crawling, shifting, rotating, somersaulting, rolling, and even fast autonomous rocking driven by a self-oscillatory motion. In addition, the highly mobile millirobots show the multifunctions of not only navigating with controllable directions but also escaping out from heavy weight and even swimming through a small pipe. It is anticipated that this photoactive and reconfigurable material system would open exciting possibilities to develop intelligent soft robots with seamless integration of multimodal shape morphing and multifunctions.

Received 30th December 2021,
Accepted 31st January 2022

DOI: 10.1039/d1tc06171b

rsc.li/materials-c

Introduction

Dynamically changing shapes in response to variations in the surrounding environment is a vital and ubiquitous functionality for biological self-adaption and survival; for example, the curvatures of Mimosa Pudica leaves and flowers for growing well^{1,2} and the reconfigurations of seedpots and pine cones for seed dispersal.^{3,4} Inspired by these biological responsive systems, artificial soft and compliant materials capable of shape morphing triggered by external stimuli (light, humidity, temperature, magnetic fields, etc.) have been developed and shown remarkable functions and properties, typically, including shape memory

polymers, hydrogels and liquid crystalline polymers.^{5–10} Programmable shape morphing of these materials has aroused great interest in emerging applications of biomedical devices, actuators and intelligent soft robots.^{11–15} In addition, the phenomenon of shape morphing originates from the internal anisotropic arrangement of the structural elements that introduce non-uniform internal stress under external stimuli,^{16,17} which induces active materials to change macroscopic shapes, such as bending, buckling, twisting, contraction, and extension.^{18,19} The complex shape-morphing behaviors, leading to various shapes (helix, wave, saddle, etc.) and patterns, can be artificially manipulated through adjusting material compositions, programming geometries and molecular orientations of the materials.^{20–22} So far, various strategies have been leveraged to realize the shape morphing of soft materials, for example, programming swelling or deswelling patterns,^{23,24} editing bilayer or multilayer structures with isotropic and anisotropic properties,^{6,20,25} and creating material gradients, such as asymmetrical crosslinking density along the thickness or spatial surface.^{26,27} However, these shape changing approaches appear complicated and hard to achieve successfully manufacturing for wide use. In most cases, the as-prepared actuators only

^a School of Materials Science and Engineering, Zhejiang University, Hangzhou 310027, China

^b Key Laboratory of 3D Micro/Nano Fabrication and Characterization of Zhejiang Province, School of Engineering, Westlake University, 18 Shilongshan Road, Hangzhou 310024, Zhejiang, China. E-mail: lyjuan@westlake.edu.cn

^c Institute of Advanced Technology, Westlake Institute for Advanced Study, 18 Shilongshan Road, Hangzhou 310024, Zhejiang, China

† Electronic supplementary information (ESI) available. See DOI: 10.1039/d1tc06171b

show simple and single shape-morphing behavior due to their low degree of freedom, which severely restricts multifunction performances. Multimodal shape morphing is ubiquitously shown by living organisms,²⁸ bringing about complex locomotions and multifunctions that enable adaptive accommodation to varying surrounding and allow for negotiation with various obstacles impossible dealt by limited morphing shapes, such as walking, swimming, and squeezing into very narrow spaces for escape and disguise.^{29–31}

Liquid crystal elastomers (LCEs) capable of reversible and large deformations through order-disorder transition of LC⁹ are remarkable anisotropic shape-morphing materials.^{8,12,31–33}

Light as a versatile stimulus allows contactless, spatial, temporal and localized control, attracting great interest of researchers to use it to gain dynamical control of shape transformation.^{19,34} Photoactive shape morphing of LCE materials has been realized through the incorporation of photochemical or photothermal elements.^{18,35} Complex shape-morphing behaviors in LCEs have been achieved through tailoring the alignment of LC mesogens by the methods of LC cells, patterns, crosslinking distribution, and 3D printing.^{19,27,36–39} However, integrating diverse shape-morphing behaviors within a single LCE actuator or robot remains a formidable challenge. To address

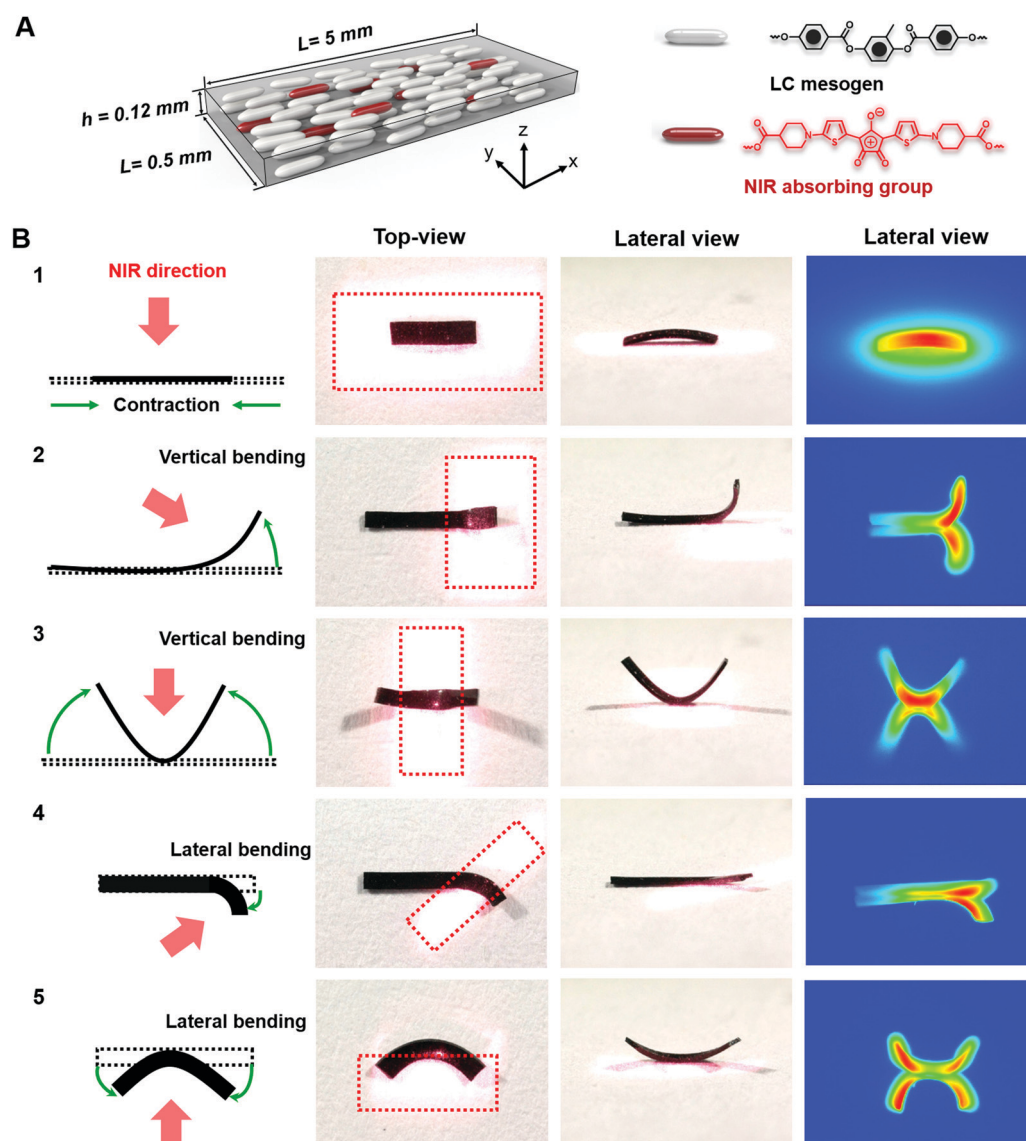


Fig. 1 Design of multiple shape morphing of NIR-active millirobots. (A) Schematics showing rectangular-sheet-shaped dimension and LC orientation profile of soft millirobots. The gray oval-shape rods and the red oval-shape rods present LC mesogens and NIR-active groups, respectively. (B) Generation of diverse 3D shape morphing. The schematic diagrams (left) show the five strategies of tailoring the incident directions of NIR light and the irradiated position of millirobot to make a millirobot shape morphing into different 3D structures. The corresponding digital photographs from top and lateral views are shown in the middle columns, and the far right column of thermal imaging shows the temperature profiles of the morphing millirobot. The black dotted lines depict the original shape and size of the robot. The green arrows indicate the shape morphing directions of the robot upon NIR irradiation. The red arrows present the incident direction of the 808 nm NIR light spot.

this challenge, several strategies have been employed. Some effective approaches are to program hierarchical structures such as bilayer structure with different functionalities individually,⁴⁰ gradient structure with various crosslinking densities³⁸ and Janus patterning structure to undergo bending, waving, and chiral twisting.^{22,41–43} Moreover, through the combination of multiple LCE materials with different responsive wavelengths and molecular orientations in an actuator, the specific domains of the composite actuators can be selectively stimulated, thus achieving multimodal shape changing.^{29,44} However, these recent progresses with increasingly complex structures and chemistries remain outweighed by great trade-offs in difficulty of fabrication and large-scale feasibility.

In this study, we present a simple and alternative driving strategy through just modulating incident light (scanning position, illumination direction and light intensity), which not only produces a broad range of desirable 3D shape morphing in a single NIR-active LCE millirobot (Fig. 1 and Movie S1, ESI†) without the need to laboriously using multiply materials, highly delicate structures or complex LC orientation patterns, but also allows local and reversible switching between diverse morphing shapes, thus enabling various locomotions, such as crawling, shifting, rotating, somersaulting, rolling, and even high-frequency rocking.

Multimodal shape morphing of millirobots

As shown in Fig. 1, the millirobot presents a rectangular-sheet shape with the dimension of 5 mm × 0.5 mm × 0.12 mm and

the uniaxial orientation (the preparation procedure described in the methods). The millirobot exhibits a relatively low glass transition temperature of ~−11 °C and nematic-isotropic transition temperature of ~70 °C (Fig. S3, ESI†). A photothermal group with stronger absorption for NIR light (Fig. S4, ESI†) is incorporated into the LCE matrix of millirobot by covalent bonding to provide high photothermal stability (Fig. 2A). Upon NIR light irradiation, the surface temperature of the millirobot can rapidly increase above the isotropic transition temperature in seconds, enabling the LCE to quickly undergo order-to-disorder transition, which results in fast and well-defined macroscopic anisotropic deformation that has great significance for robotic applications.⁴⁵

Owing to high flexibility and unlimited degrees of freedom for the used LCE material, the millirobot can be photomanipulated to generate various time-varying shapes.⁴⁴ As depicted in Fig. 1B and Movie S1 (ESI†), tailoring the direction and location of NIR irradiation, the millirobot can be controlled by one light spot to generate different shape-morphing modes. Alternatively, both the incident direction of NIR spot and the irradiated position of the millirobot determine and produce spatially varying temperature profiles and order gradients of LCE mesogens, leading to corresponding varying stress and strain distribution and allowing millirobots to spontaneously generate time-varying shape morphing. To clearly exhibit shape morphing of the 3D structure of the photoactive millirobot, the schematics illustrating the formation of the 3D structure and the relationships between the incident directions of NIR light

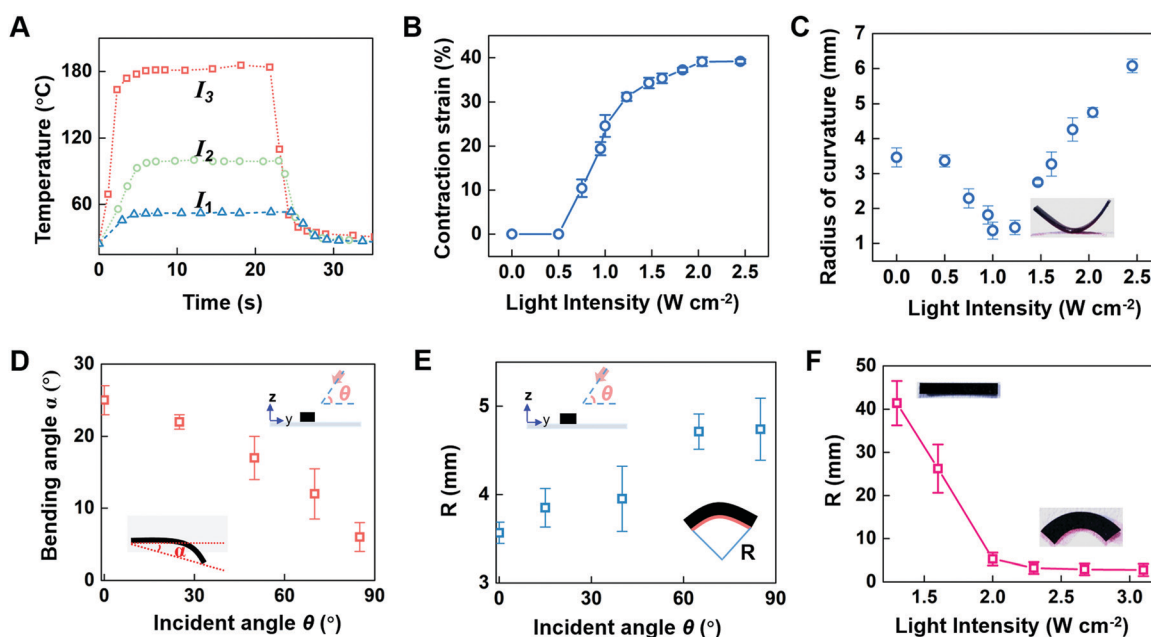


Fig. 2 (A) The effect of the NIR light intensity on the surface temperature of millirobot. I_1 , I_2 , and I_3 are corresponding to 1, 2, and 3 W cm^{−2}, respectively. (B) The relationship between light intensity and contraction strain of the millirobot along the direction of nematic director. (C) The changes in the radius of curvature influenced by light intensity for morphing mode 3. (D) The influences of the incident angle of the NIR light on the lateral bending angle in morphing mode 4. The insets show corresponding schematics that demonstrate incident angle of the NIR light and bending angle of the millirobot. Light intensity is ~2 W cm^{−2}. (E) The effects of the incident angle on the radius of curvature in morphing mode 5. The insets schematically show incident angle of the NIR light and the radius of curvature. Light intensity is ~2 W cm^{−2}. (F) The changes of the radius of curvature versus light intensity in morphing mode 5. The incident angle of NIR light is ~10°.

and the irradiated position on the millirobot have been shown in Fig. 1B (left). The top view and the corresponding side view of the shape morphing 3D structures of the millirobot are also presented. Moreover, to identify the correlation between shape morphing and temperature distribution, the thermal imaging of top and side views of the millirobot are exhibited in Fig. S6 (ESI†) and Fig. 1B, respectively. The temperature profiles detected by thermal imaging show the location of the NIR spot and the irradiated position of the millirobot. When the millirobot is exposed and fully covered by an NIR spot, it contracts immediately along the direction of long axis and bend downwards slightly to form first 3D structure (morphing mode 1 in Fig. 1B), and the maximum contraction strain is about 39%. The effect of light intensity on the contraction ratio has been further identified, as shown in Fig. 2B. To create partial 3D morphing, a part of the millirobot is locally stimulated by a NIR spot. When the light source located at the upper left of the

robot illuminates the right end of the robot, it not only undergoes partial contraction but also partially bends up, generating the second 3D structure with asymmetric feature (morphing mode 2 in Fig. 1B). In addition, changing the location of the NIR spot, when the center of the millirobot is stimulated, a large "V" shape deformation (morphing mode 3 in Fig. 1B) can be formed; Fig. 2C exhibits detail relationships between light intensity and the radius of curvature. During the contraction of the center, the millirobot initially deforms into "V" shape that the radius of curvature initially depresses and then sharply improves during the increase of light intensity, attributing to asymmetrical strain profile along the thickness direction induced by temperature gradient, which is echoed by thermal imaging profile. The larger intensity produces higher temperature, leading to the depression of temperature gradient and causing the increase in the radius of curvature of "V" shape. Moreover, when NIR light irradiates the lateral side of the

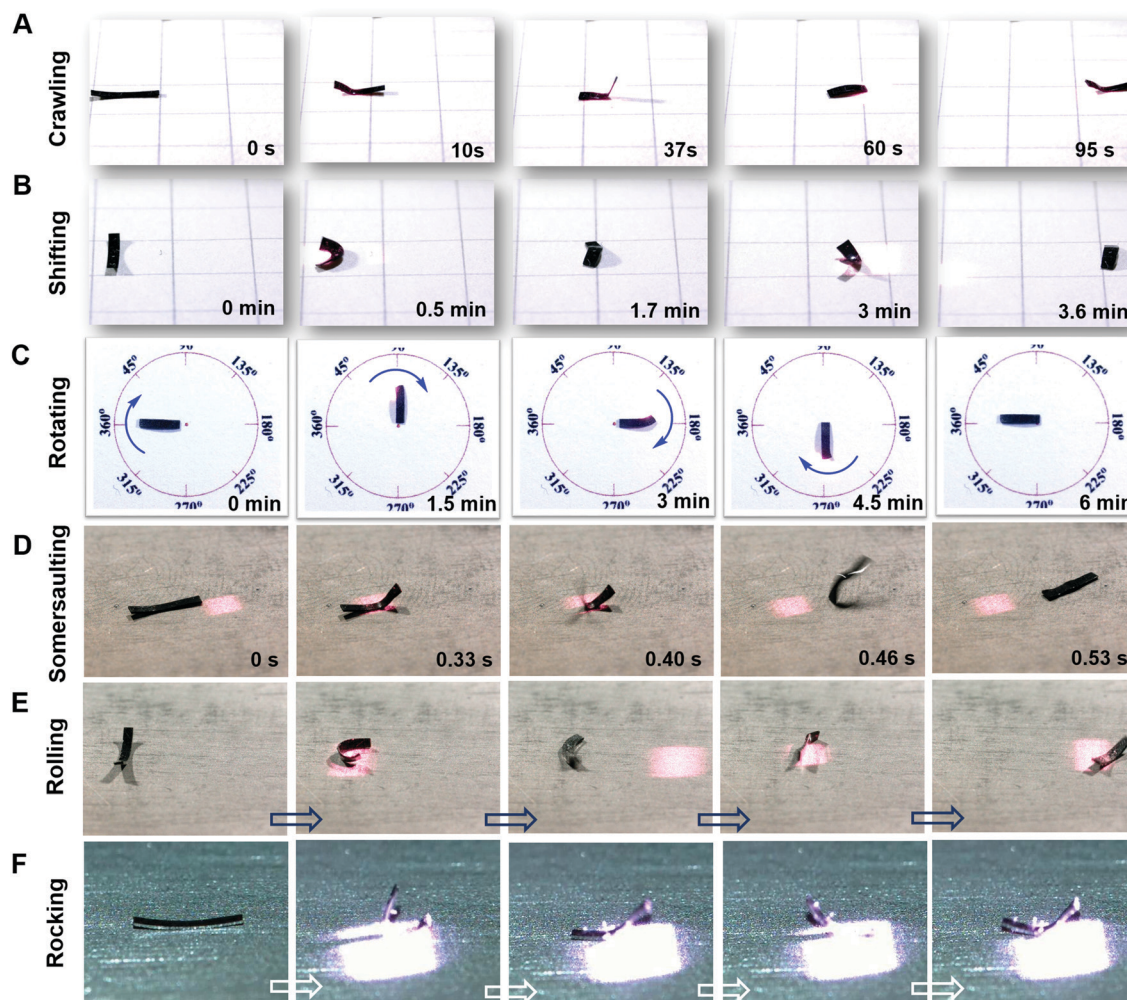


Fig. 3 Multimodal locomotion. (A) The millirobot crawled forward under the repeatedly and directionally scanning of the NIR spot. The crawling direction is consistent with the scanning direction of the NIR spot. (B) The millirobot shifted forward upon the irradiation of the NIR light on the lateral side of the millirobot's body. (C) The millirobot rotated 360° upon the irradiation of a tilted NIR spot. The size of millirobot is 3 mm × 0.5 mm × 0.12 mm. (D) The millirobot exerted somersaulting with the aid of the NIR spot scanning. (E) The millirobot rolled forward upon the irradiation of the NIR spot whose long axis is parallel to that of the robot. (F) Fast-rocking behavior, a novel self-oscillating movement shown by the millirobot when the center of its body is illuminated by incident NIR light. The size of the millirobot is 5 mm × 0.5 mm × 0.12 mm. The intensity of the NIR light is 1–3 W cm⁻².

millirobot in a tilted manner relative to the millirobot's long axis, it can produce lateral bending behavior, presenting non-plane "J" shape and forming the fourth 3D structure (morphing mode 4 in Fig. 1B). The degree of the lateral bending of the "J" shape is dependent on the incident angle, as demonstrated in Fig. 2D. The incident light with small tilted angles results in larger thermal gradient and strain gradient along the *y*-axis (Fig. 1B), inducing lateral bending with larger angle. When incident NIR light fully covers one lateral side of the millirobot, the millirobot laterally bends into a "C" shape as observed from the top view (morphing mode 5 in Fig. 1B). From the side view, both ends of the millirobot bend upwards. The radius of curvature of the lateral bending in morphing mode 5 can be tailored through controlling the incident angle of NIR (Fig. 2E). The smaller incident angle used, the larger thermal temperature gradient and strain gradient along *y*-axis arises simultaneously. In addition, the effect of light intensity on the radius of curvature of the "C" shape has also been analyzed in Fig. 2F. These diverse shape morphing allows the millirobot to perform selective contraction, bending and shape change into 3D "J", "V" and "C" shapes without using complicated program and patterns of the LC orientation field. It is noteworthy to mention that all these shape transformations can self-recover to the initial shape when NIR irradiation is turned off without any aid of artificial intervention or the second light irradiation.

Multimodal locomotion of millirobots

Owing to a broad range of tunable shape morphing controlled by the location and direction of NIR light, the multimodal locomotion of millirobots can be achieved including crawling, shifting, rotating, somersaulting, rolling, and rocking locomotion, as shown in Fig. 3 and Movies S2, S3 (ESI[†]). By steering the NIR spot, scanning from one end of a millirobot to another end periodically and directionally, the millirobot demonstrates directional crawling behavior (Fig. 3A). The crawling mechanism includes two stages, as analyzed in Fig. S7 (ESI[†]). In the first stage, the NIR spot induces one end of the millirobot bending up and shrinking. As the NIR spot moves forward, another end of the millirobot gradually follows shape morphing of bending up and shrinking. In addition, one scanning cycle from the one end to another end results in the full contraction of the entire body. In the second stage after the NIR spot moved off the millirobot, the contracted millirobot elongates along the robot's long axis and buckles into an arched shape attributing to the elongation induced by the decreasing temperature of the robot. Finally, one end of the millirobot extends and pushes the robot forward, displaying crawling behavior. Furthermore, changing the incident direction of the NIR spot, using the morphing mode 5 shown in Fig. 1B, a novel locomotion of shifting can be created (Fig. 3B). When the NIR spot irradiates from the lateral side of the robot, it transforms its shape from the planar structure into a 3D "C" shape, producing an effective motion to move forward with a shifting gait (Fig. S8, ESI[†]). In addition, applying the tilted NIR

spot, the irradiated millirobot changes its shape into an asymmetric "J" architecture, as depicted in Fig. 1B (morphing mode 4). Depending on this 3D shape morphing, the deflection of the robot body allows 360° rotation in favor of direction turning for the moving millirobot (Fig. 3C). Interestingly, when the applied NIR spot rapidly scans a millirobot, the millirobot rapidly changes its shape into a curved structure to accumulate and convert light-induced thermal energy into a forward rolling motion, driving millirobots somersaulting (Fig. 3D). Lateral rolling can also be achieved by our millirobots when NIR light stimulates the lateral side of the robot (Fig. 3E). As shown in Fig. S11 (ESI[†]), when the lateral side of the millirobot is exposed to the NIR light, the body shrinks, forming a "C" shape with an unstable state, continuous NIR irradiation leads the deformed millirobot to flipping, thus exhibiting a lateral rolling behavior. Even more impressively, a fast-rocking behavior is exhibited by the millirobot, which is a kind of self-sustained oscillating motion with a high frequency up to 12 Hz, when the center of the millirobots is illuminated by the incident NIR light (Fig. 3F). Moreover, the self-oscillating millirobot can autonomously follow the moving NIR spot with unchanged intensity and incident angle. This novel autonomous rocking behavior driven by self-oscillation has not been previously reported until now, which may permit a particular function.

Multifunctions of millirobots

Multimodal locomotion not only provides unprecedented advantages to robotic mobility but also offers excellent adaptation to various environments. Besides the agile locomotion in dry environment, based on the fundamental shape morphing, our millirobots can serve as aquatic soft robots interacting with fluid-immersed media (*e.g.* water) and enabling diverse locomotion under water-like aquatic invertebrates;⁴⁶ for instance, sea slugs and snails, as shown in Fig. 4C and Fig. S14 (ESI[†]). Free moving is the dominant locomotion for sea creatures on the seabed. For our millirobots, NIR light illumination at one end of the millirobot can result rapid bending, forming a motion of flapping water (Fig. 4C and Movie S6, ESI[†]), which can overcome higher drag force and generate propulsion to drive millirobots moving forward. In addition to flapping water to induce moving, the millirobot is capable of somersaulting and floating under water, as shown in Fig. S14 (ESI[†]). With the aid of the supportive buoyancy of water and larger shape morphing of the millirobot, the millirobot undergoes somersaulting behavior facilely.

As demonstrated above, multimodal locomotion within only one millirobot can be achieved from the agile control of the incident NIR light. In addition to robust locomotion capability, the millirobots possess unique and outstanding functions like numerous organisms.⁴⁷ Tailoring the distribution of NIR, namely, the direction and location, we can actively control the shape morphing of millirobots. Hence, for shifting locomotion, the moving direction can be turned by tuning the position

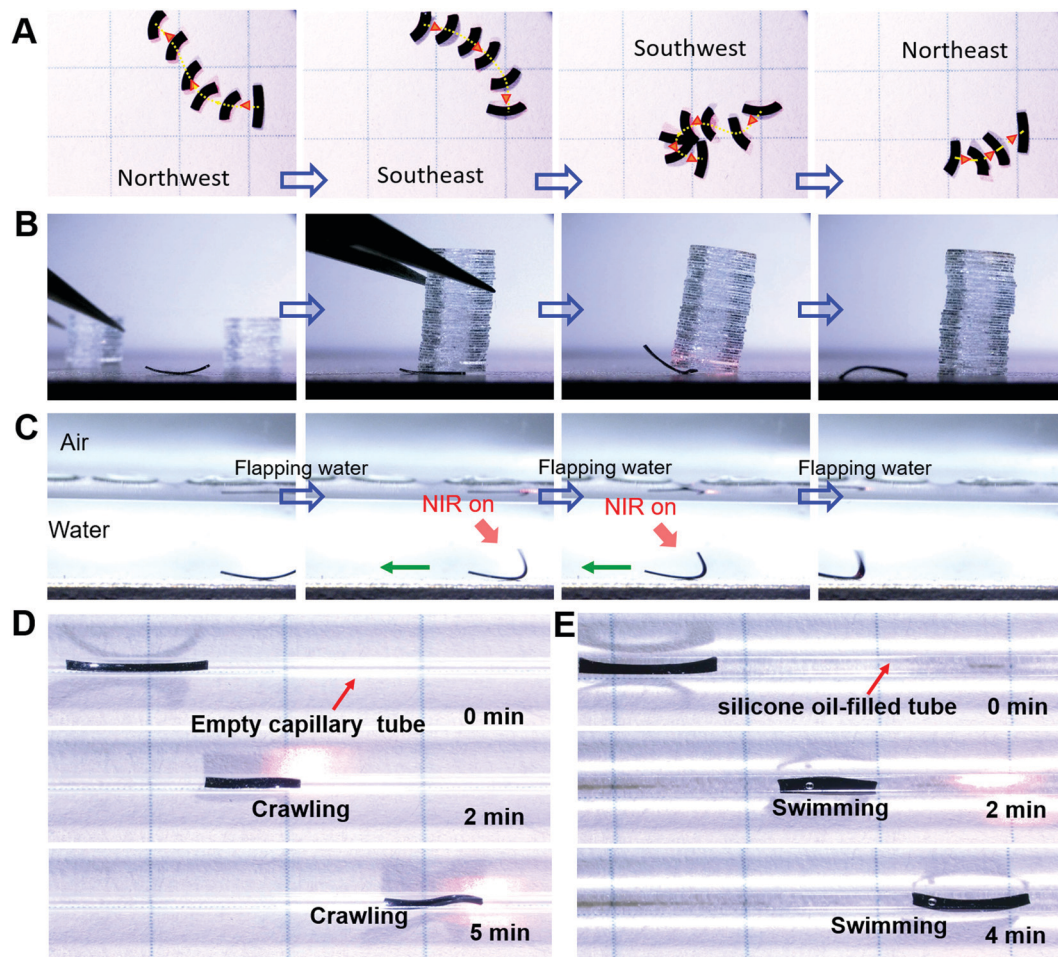


Fig. 4 Multifunctions. (A) The millirobot underwent flexible shifting in various directions controlled by NIR light. (B) The millirobot (weight 0.3 mg) pressed under a stack of glass sheets (weight 388.4 mg) can perform shape morphing and escape out. (C) Underwater locomotion performances. NIR spot induces millirobot partially bending and flapping water, leading to moving forward. The millirobot crawled inside a glass tube with (E) or without (D) silicone oil. The size of the millirobot is $5 \times 0.5 \times 0.12 \text{ mm}^3$. The intensity of the NIR light is $1\text{--}3 \text{ W cm}^{-2}$.

of the NIR light with respect to the center of the structure. As illustrated in Fig. S9 (ESI†), when the long axis of the NIR spot is parallel to that of the millirobot, both ends of the millirobot undergo symmetrical deformation, yielding forward-shifting motion. When the tilted NIR spot was used, the millirobot experiences large asymmetrical shape morphing, resulting in the turning of shifting direction. Based on such steering strategy, we can flexibly steer the millirobot to navigate along a desired pathway on demand. As demonstrated in Fig. 4A and Movie S4 (ESI†), our millirobot can be flexibly steered in various directions through the modulation of NIR light. Moreover, as shown in Fig. S12 (ESI†), the millirobots can exert shifting locomotion through an “S” pathway to traverse through obstacles, demonstrating a versatile and precise two-dimensional manipulation over the millirobots. Beside the versatile locomotion, our millirobots own considerable robustness and actuation stress. As shown in Fig. 4B and Movie S5 (ESI†), a millirobot of 0.3 mg can pry up a stack of glass sheets with a weight up to 388.4 mg, which is about 1295 times heavier than the mass of the robot. Moreover, fueled by NIR light, the robot

can undergo contraction and extension shape morphing to crawl under the weight, exhibiting functions that help the millirobot to move under heavy loadings and then successfully escape out from heavy glass sheets finally owing to its powerful actuation (Fig. S13, ESI†). The actuation stress of the robot can reach up to $\sim 1.8 \text{ MPa}$, much higher than that of the skeletal muscle (0.35 MPa). In addition, the millirobot can crawl through a glass tube full of silicone oil that can generate strong fluid resistance to severely hinder mobility, demonstrating flexible morphing capabilities to adapt to complex varying environments (Fig. 4E, F and Movie S7, ESI†). For most developing LCE actuators and shape-morphing materials, those functions mentioned above could not be achieved in a single actuator.^{48,49}

Conclusion

In summary, we have developed an effective approach of manipulating incident light to gain controllable multiple shape-morphing behaviors in a photoactive LCE material.

Namely, the spatial, temporal, and localized features of the optical manipulation have been leveraged to program light-induced strain gradients in the material, and thus achieved dynamically shape morphing and reconfiguration. The predictable shape-morphing of millirobots by programming the magnitude and direction of the strain gradients in the LCE actuator with constant orientation enable the robots to exert various shape morphing upon dynamic optical stimulation. Through the spatiotemporally dynamic manipulation, the millirobots enable shape morphing into diverse structures in response to the incident light with varying directions and locations. By combining different basic modes of shape morphing, a variety of controllable locomotions can be collectively conducted in a single millirobot, which few photo-driven soft robots can achieve in previous reports. Such an intelligent LCE material system integrated with an almost limitless number of 3D morphing shapes might be useful in the applications of hyper-abundant robots, actuation devices, wireless sensors, and microfluidic devices.

Experimental section

Fabrication of LCE and millirobots

The LCE with uniaxial orientation was prepared by two-step polymerization *via* thiol-ene click chemistry. First, the mixture of RM82 (200 mg, 297.28 mmol, 98%, Bayi Space), NIR-monomer (31.38 mg, 33.03 mmol), DODT (43.01 mg, 235.93 mmol, 97%, TCI), PETMP (23.06 mg, 47.19 mmol, 90%, TCI) were dissolved in 2 mL dichloromethane (DCM). Thiol groups and acrylate groups were equimolar for above mixture. After that, one drop of dipropylamine (DPA, 99%, Adamas) was added into the solution of mixture. Then, the mixture was transferred into a custom-made Teflon mold (3 cm × 3 cm × 0.5 cm) quickly. After 5 h at room temperature, the pre-crosslinking LCE film formed and was stretched to 50% strain, secondly, keeping for 24 h to complete the crosslinking reaction and fix the orientation of the LCE film with an average thickness about 120 μm. An uniaxially oriented LCE was cut into many small rectangular sheets (5 mm × 0.5 mm × 0.12 mm) whose long axis parallel to the nematic director *n*. These small rectangular sheets have been used and developed as millirobots.

Characterization

The differential scanning calorimetry (DSC) measurement was carried out by a TA Instruments DSC250 at a heating rate of 10 °C min⁻¹ in a nitrogen atmosphere. The UV-Vis-NIR absorption spectra of the NIR monomer in dichloromethane solution and LCE film were recorded using a Shimadzu UV-2700 spectrophotometer. Infrared thermal imager instrument (FLIR-A600-Series, Sweden) was used to observe NIR-induced thermal distribution and intensity. Photomechanical forces were measured using tensile machine of Instron 5943. For all NIR-light-driven experiments, an NIR laser source with a wavelength of 808 nm was employed. Laser power was measured by a power meter (CNI, HS1 + TP100). Two-dimensional (2D) WAXD

experiments were carried out on a Bruker D8 Venture diffractometer with a PHOTON III detector with an incoatec micro-focus source (Cu K α , $\lambda = 1.5418 \text{ \AA}$) equipped with an Oxford 800 Plus liquid nitrogen vapor cooling device. The photographs and videos of the NIR-light-driven experiments were recorded by a super-resolution digital microscope (Keyence, VHX-6000). The video of oscillation behavior was recorded by a high-speed microscope VW-9000.

Conflicts of interest

The authors declare no competing interests.

Acknowledgements

This research was supported by National Natural Science Foundation of China (51873197), 151 Talent Project of Zhejiang Province, and Foundation of Westlake University.

References

- 1 A. G. Volkov, J. C. Foster, T. A. Ashby, R. K. Walker, J. A. Johnson and V. S. Markin, *Plant, Cell Environ.*, 2010, **33**, 163–173.
- 2 H. W. Krenn, *Annu. Rev. Entomol.*, 2010, **55**, 307–327.
- 3 R. M. Erb, J. S. Sander, R. Grisch and A. R. Studart, *Nat. Commun.*, 2013, **4**, 1–8.
- 4 A. R. Studart, *Angew. Chem., Int. Ed.*, 2015, **54**, 3400–3416.
- 5 C. Ma, X. Le, X. Tang, J. He, P. Xiao, J. Zheng, H. Xiao, W. Lu, J. Zhang, Y. Huang and T. Chen, *Adv. Funct. Mater.*, 2016, **26**, 8670–8676.
- 6 S. Janbaz, R. Hedayati and A. A. Zadpoor, *Mater. Horiz.*, 2016, **3**, 536–547.
- 7 Y. Alapan, A. C. Karacakol, S. N. Guzelhan, I. Isik and M. Sitti, *Sci. Adv.*, 2020, **6**, eabc6414.
- 8 Y. Kim, H. Yuk, R. Zhao, S. A. Chester and X. Zhao, *Nature*, 2018, **558**, 274–279.
- 9 M. Li and P. Keller, *Philos. Trans. R. Soc., A*, 2006, **364**, 2763–2777.
- 10 L. Zhang, Y. Zhang, F. Li, S. Yan, Z. Wang, L. Fan, G. Zhang and H. Li, *ACS Appl. Mater. Interfaces*, 2019, **11**, 12890–12897.
- 11 C. Ma, S. Wu, Q. Ze, X. Kuang, R. Zhang, H. J. Qi and R. Zhao, *ACS Appl. Mater. Interfaces*, 2021, **13**, 12639–12648.
- 12 Q. He, Z. Wang, Y. Wang, A. Minori, M. T. Tolley and S. Cai, *Sci. Adv.*, 2019, **5**, 1.
- 13 H. Xie, M. Sun, X. Fan, Z. Lin, W. Chen, L. Wang, L. Dong and Q. He, *Sci. Robot.*, 2019, **4**, eaav8006.
- 14 H. Arazoe, D. Miyajima, K. Akaike, F. Araoka, E. Sato, T. Hikima, M. Kawamoto and T. Aida, *Nat. Mater.*, 2016, **15**, 1084–1089.
- 15 M. Pilz da Cunha, S. Amberg, M. G. Debije, E. F. Homburg, J. M. den Toonder and A. P. Schenning, *Adv. Sci.*, 2020, **7**, 1902842.

- 16 R. K. Manna, O. E. Shklyaev, H. A. Stone and A. C. Balazs, *Mater. Horiz.*, 2020, **7**, 2314–2327.
- 17 I. Apsite, A. Biswas, Y. Li and L. Ionov, *Adv. Funct. Mater.*, 2020, **30**, 1908028.
- 18 A. S. Kuenstler and R. C. Hayward, *Curr. Opin. Colloid Interface Sci.*, 2019, **40**, 70–86.
- 19 G. Stoychev, A. Kirillova and L. Ionov, *Adv. Opt. Mater.*, 2019, **7**, 1900067.
- 20 P. Xue, H. K. Bisoyi, Y. Chen, H. Zeng, J. Yang, X. Yang, P. Lv, X. Zhang, A. Priimagi, L. Wang, X. Xu and Q. Li, *Angew. Chem., Int. Ed.*, 2021, **60**, 3390.
- 21 J. Cui, T. Y. Huang, Z. Luo, P. Testa, H. Gu, X. Z. Chen, B. J. Nelson and L. J. Heyderman, *Nature*, 2019, **575**, 164–168.
- 22 L. Yu, H. Shahsavan, G. Rivers, C. Zhang, P. Si and B. Zhao, *Adv. Funct. Mater.*, 2018, **28**, 1802809.
- 23 J. H. Na, N. P. Bende, J. Bae, C. D. Santangelo and R. C. Hayward, *Soft Matter*, 2016, **12**, 4985–4990.
- 24 Y. Zhao, C. Xuan, X. Qian, Y. Alsaid, M. Hua, L. Jin and X. He, *Sci. Robot.*, 2019, **4**, eaax7112.
- 25 J. Zhang, Y. Guo, W. Hu, R. H. Soon, Z. S. Davidson and M. Sitti, *Adv. Mater.*, 2021, **33**, 2006191.
- 26 F. Ge and Y. Zhao, *Adv. Funct. Mater.*, 2020, **30**, 1901890.
- 27 Z. Wang, Z. Wang, Y. Zheng, Q. He, Y. Wang and S. Cai, *Sci. Adv.*, 2020, **6**, eabc0034.
- 28 K. H. Low, T. Hu, S. Mohammed, J. Tangorra and M. Kovac, *Bioinspiration Biomimetics*, 2015, **10**, 020301.
- 29 Y. Huang, H. Bisoyi, S. Huang, M. Wang, X. M. Chen, Z. Y. Liu, H. Yang and Q. Li, *Angew. Chem., Int. Ed.*, 2021, **60**, 11247–11251.
- 30 X. Du, H. Cui, T. Xu, C. Huang, Y. Wang and Q. Zhao, *Adv. Funct. Mater.*, 2020, **30**, 1909202.
- 31 B. E. Treml, R. N. McKenzie, P. Buskohl, D. Wang, M. Kuhn, L. S. Tan and R. A. Vaia, *Adv. Mater.*, 2018, **30**, 1705616.
- 32 Z. Mao, K. Zhu, L. Pan, G. Liu, T. Tang, Y. He, J. Huang, J. Hu, K. W. Y. Chan and J. Lu, *Adv. Mater. Technol.*, 2020, **5**, 1900974.
- 33 T. Xu, J. Zhang, M. Salehizadeh, O. Onaizah and E. Diller, *Sci. Robot.*, 2019, **4**, eaav4494.
- 34 H. Kim, J. Kang, Y. Zhou, A. S. Kuenstler, Y. Kim, C. Chen, T. Emrick and R. C. Hayward, *Adv. Mater.*, 2019, **31**, 1900932.
- 35 L. Dong and Y. Zhao, *Mater. Chem. Front.*, 2018, **2**, 1932–1943.
- 36 S. Ahn, T. H. Ware, K. M. Lee, V. P. Tondiglia and T. J. White, *Adv. Funct. Mater.*, 2016, **26**, 5819–5826.
- 37 Y. Wang, A. Dang, Z. Zhang, R. Yin, Y. Gao and L. Feng, *Adv. Mater.*, 2020, **32**, 2004270.
- 38 Y. Xiao, Z. Jiang, J. Hou and Y. Zhao, *Nat. Commun.*, 2021, **12**, 1–10.
- 39 L. T. De Haan, A. P. H. J. Schenning and D. J. Broer, *Polymer*, 2014, **55**, 5885–5896.
- 40 Y. Y. Xiao, Z. C. Jiang, X. Tong and Y. Zhao, *Adv. Mater.*, 2019, **31**, 1903452.
- 41 H. Kim, S. Ahn, D. M. Mackie, J. Kwon, S. H. Kim, C. Choi, Y. H. Moon, H. B. Lee and S. H. Ko, *Mater. Today*, 2020, **41**, 243.
- 42 T. van Manen, S. Janbaz and A. A. Zadpoor, *Mater. Today*, 2018, **21**, 144–163.
- 43 T. H. Ware, J. S. Biggins, A. F. Shick, M. Warner and T. J. White, *Nat. Commun.*, 2016, **7**, 1–7.
- 44 B. Zuo, M. Wang, B. Lin and H. Yang, *Nat. Commun.*, 2019, **10**, 4539.
- 45 J. Wang, D. Gao and P. S. Lee, *Adv. Mater.*, 2020, **32**, 2003088.
- 46 L. Daler, S. Mintchev, C. Stefanini and D. Floreano, *Bioinspiration Biomimetics*, 2015, **10**, 016005.
- 47 S. Mintchev and D. Floreano, *IEEE Robot. Autom. Mag.*, 2016, **23**, 42–54.
- 48 Z. Nie, B. Zuo, M. Wang, S. Huang, X. M. Chen, Z. Y. Liu and H. Yang, *Nat. Commun.*, 2021, **12**, 2334.
- 49 Z. Liu, H. K. Bisoyi, Y. Huang, M. Wang, H. Yang and Q. Li, *Angew. Chem., Int. Ed.*, 2021, e202115755.